# Oxygen Chemistry in Polymer Fouling: Insights from Multiphase Detailed Kinetic Modeling

Hao-Wei Pang, Xiaorui Dong, and William H. Green*

*Department of Chemical Engineering, Massachusetts Institute of Technology, Cambridge, Massachusetts 02139, United States*

E-mail: whgreen@mit.edu

**Abstract**

Polymer fouling is a pervasive challenge in downstream processes of steam cracking. Molecular oxygen is likely to present and known to strongly affect various polymerization processes, yet the role of oxygen in distillation column fouling remains poorly understood. Building upon the foundations laid in our preceding study [Pang et al., *Ind. Eng. Chem. Res.* 2023, 62, 36, 14266–14285], this work presents a detailed kinetic modeling approach to investigate the impact of oxygen on polymer fouling in a typical debutanizer. The fouling model incorporates molecular oxygen as a primary source of contamination in the feedstock and encompasses a comprehensive network of chemical reactions, phase equilibria, and interphase transport phenomena. Critical model parameters are derived from quantum chemistry calculations to ensure accuracy. The sensitivity of fouling rates to varying levels of dissolved oxygen is examined. We find that even small traces (ppb level) of molecular oxygen contaminant in the feedstock can significantly accelerate fouling growth in the colder section. Furthermore, the dominant pathways of fouling are observed to shift over time due to diffusion limitations. This study showcases the power and adaptability of predictive detailed kinetic modeling in deciphering the mechanistic fundamentals of polymer fouling.

# 1 Introduction

Polymer fouling is a complex and significant challenge in the chemical industry that can cause reduced efficiency, increased downtime, and safety risks, all with high economic costs. Despite being a recognized issue for decades, the fundamental origins of polymer fouling remain unclear, and mitigation strategies are primarily empirical. Moreover, researchers haven't agreed upon the fouling mechanism, fouling precursors, and the location of reactions (in the bulk liquid or at the equipment surface).[1] Additionally, very few predictive detailed models exist for polymer fouling. Oftentimes, the fouling models are composed of pseudo-species or highly simplified chemistry,[2–5] which loses the resolution to investigate chemical mechanistic details.

In our prior research, we took the initial step of creating a predictive multiphase detailed chemical kinetic model for polymer fouling in an industrial distillation column that separates C4 and lighter species from heavier ones ("debutanizer"),[6] as illustrated in Fig. 1. That model only considered the base case scenario, which includes alkanes, alkenes, conjugated dienes, and aromatics from steam cracker effluents, and excluded any impurities or industrial additives. The model showed that under the base case scenario, the main fouling mechanism is the polymerization of reactive monomers, *e.g.*, dienes. Moreover, the model illustrated that under the base case scenario, fouling growth is primarily caused by reactions in the thin film on the tray surface, while reactions in the bulk liquid are crucial for controlling the concentration of reactive intermediates (*e.g.*, radicals) involved in the surface reactions. That prior work suggests that predictive detailed modeling can be the key to reaching a scientific consensus on fouling fundamentals.

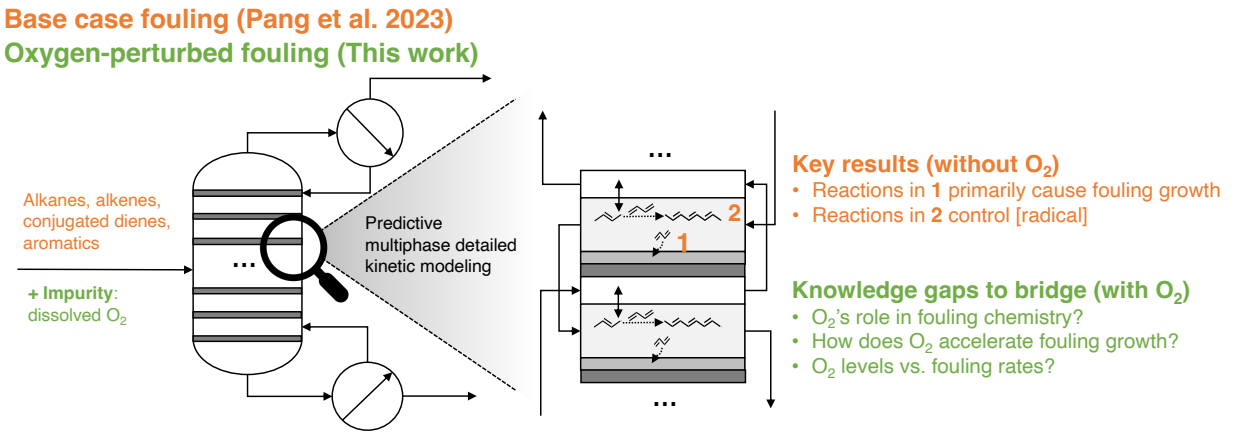


Figure 1: Schematic of key results from our prior work[6] and knowledge gaps this work aims to bridge.

Impurities can greatly impact the fouling chemistry. One of the most prevailing impurities is traces of dissolved oxygen in the unit fluid, which can enter the process as an impurity along with the feedstock, water used for quenching, or additives. Literature experimental investigations have shown that dissolved oxygen can affect fouling significantly,[7–12] where dissolved oxygen was measured to accelerate fouling[7,12] even at ppm level concentrations,[10] while the fouling rate becomes independent of oxygen concentration near air-saturation.[12] The effects of dissolved oxygen on fouling rates were recently measured using Quartz Crystal Microbalance with Dissipation monitoring (QCM-D), similar to the prediction by our detailed fouling model for QCM-D cell fouling.[6]

It is generally accepted that oxygen affects fouling through autoxidation.[8–10,13] Autoxidation is a process where dissolved oxygen combines with ordinary radicals formed from reactions between unsaturated hydrocarbons, transforming into peroxyl radicals. The peroxyl radicals then propagate with additional monomers and dissolved oxygens and become polyperoxides, which eventually become oxygenated deposits. For certain monomers, the autoxidation forms peroxyl radicals that are more reactive than the ordinary radicals, accelerating the fouling process. However, the relative rates of fouling contributed by ordinary radical polymerization and autoxidation depend on the specific fouling monomers involved. The threshold oxygen concentration at which autoxidation begins to dominate is not well

understood for many fouling monomers, let alone for mixtures. Fouling in an industrial distillation column is a much more complicated phenomenon. The interplay between the detailed chemistry of the dissolved oxygen and the complex mixture of species in feedstock, the wide range of tray temperatures (which affects the kinetics), the convective flow, the vapor-liquid mass transfer, and the phase equilibria in industrial units are not well-understood.

In this work, we extend the base case model for debutanizer fouling in our previous work toward oxygen chemistry ("oxygen-perturbed model"), as illustrated in Fig. 1. We follow a similar modeling method as presented in our previous work.[6] A general flow sheet of this work can be found in Fig. 2. First, we model the separation chain downstream of the steam cracker using Aspen Plus,[14] where we introduce dissolved oxygen to the debutanizer feedstock at an air-saturated concentration for the extreme-case scenario study. We generate the polymerization and autoxidation mechanism in the bulk liquid at each tray, condenser, and reboiler, using Reaction Mechanism Generator (RMG),[15–18] a software package for automatic mechanism generation, originally developed by the MIT Green Group, and now developed as an open-source project. To obtain a mechanism with a reasonable size, we use a hard cutoff for oligomer size during mechanism generation. We want to recover the chemistry related to the truncated larger oligomers. The Anderson-Schulz-Flory (ASF) distribution is an expression that predicts the weight distribution of oligomers with respect to its number of monomer units,[19] developed from ideal chain-growth polymerization. Using the ASF distribution, we can estimate the concentration of truncated larger oligomers based on those of the smaller oligomers in the mechanism. We modify the ASF distribution expression to accommodate the combination of ordinary free radical polymerization and autoxidation to better estimate the oligomer distribution under molecular oxygen contamination. The film growth mechanism at the surface of each tray, condenser, and reboiler is modeled using a variant of fragment-based modeling,[20] a type of lumping well-suited for modeling unselective chemistry of mixtures containing macromolecules. We update the fragment-based reaction template presented previously[6] to include important autoxidation reactions. We simulate

the oxygen-perturbed fouling model with a simulation scheme similar to our previous work[6] using ReactionMechanismSimulator.jl (RMS),[21,22] a Julia software package for simulating large chemical kinetics models developed recently by the MIT Green Group. As shown below, the new oxygen-perturbed model predicts a faster fouling rate in some trays of the column and prompts us to consider diffusion limits when simulating the fouling growth.

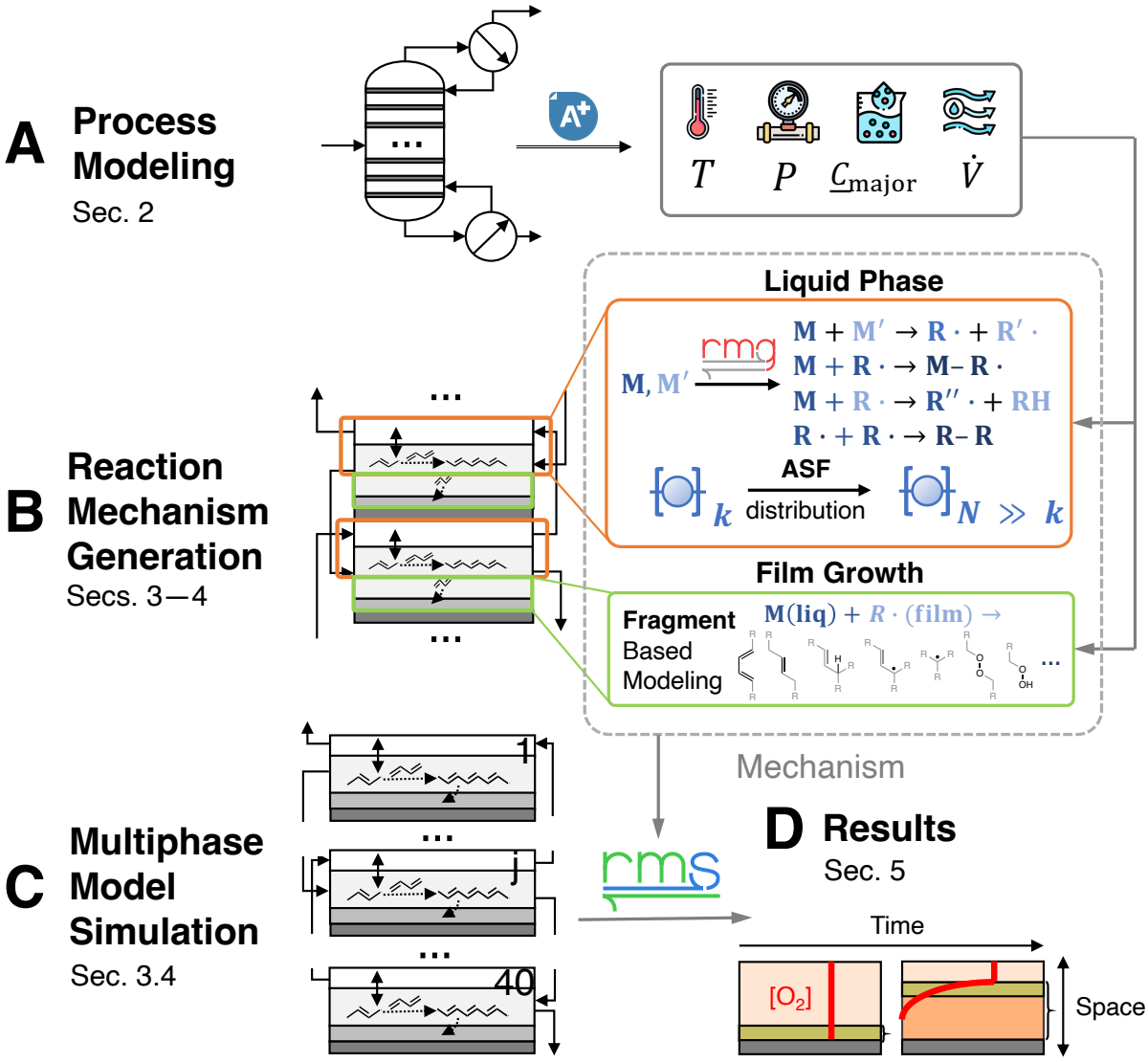


Figure 2: General flow sheet of this work.

## 2 Obtaining reaction and flow conditions affecting polymer fouling from Aspen modeling

We use an Aspen model of the separation chain downstream of the steam cracker to investigate the reaction and flow conditions around which polymer fouling occurs, and study the dissolved oxygen concentrations in the distillation column of interest. The debutanizer column is downstream of a depropanizer, so the feed is a C4+ mixture. The biggest component is butadiene, but it also contains benzene, cyclopentadiene, and other compounds. We modify the Aspen model from our previous work[6] and introduce various oxygen concentrations to the debutanizer feed, up to that it contains an air-saturated level of dissolved oxygen as an upper bound. Since we weren't able to find experimental data for oxygen solubility in butadiene, we approximate it using the saturated concentration of $O_2$ in benzene (1.9 mol of $O_2$ per $m^3$ of benzene)[23].

The major species concentration, dissolved oxygen concentration, and the temperature at each tray, the condenser, and the reboiler in the debutanizer are shown in Fig. 3, where the feed to the debutanizer contains an air-saturated level of dissolved oxygen. Aspen simulation shows that dissolved oxygen in the feedstock gets distilled out and results in a higher concentration of oxygen in the top part of the column. The $O_2$ concentration decreases drastically in the bottom section. Concentrations below $10^{-18}$ mol/$m^3$ in the Aspen output show numerical noise and are set to zeros in the subsequent steps of the modeling.

For the major species, the reactions in this system are slow compared with the flows, so the reactions do not significantly affect their concentrations. Although the $O_2$ concentration is much smaller than some major species, its steady-state concentrations in each tray are majorly determined by the relatively fast flow, including $O_2$ evaporation, and are not significantly affected by reactions.

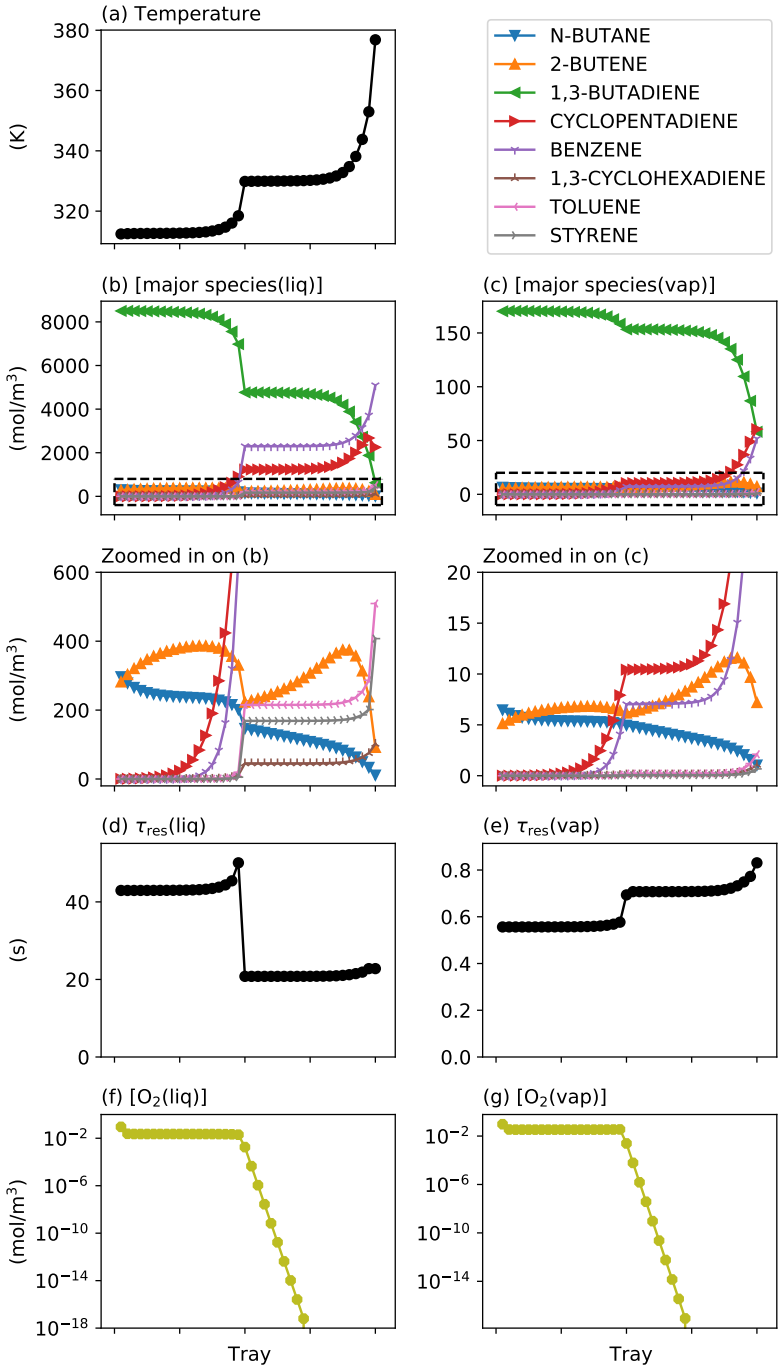


Figure 3: Temperature (a), major species concentrations in the bulk tray liquid (b) and tray overhead vapor (c), the residence time of the bulk tray liquid (d) and the tray overhead vapor (e), and oxygen concentration in the bulk tray liquid (f) and tray overhead vapor (g) at different locations in the debutanizer as computed using Aspen Plus. Tray 1 refers to the condenser, tray 40 refers to the reboiler, and tray 20 is the feed tray. The residence time of the liquid/overhead vapor is calculated as the liquid/vapor phase volume divided by the liquid/vapor outlet flowrate. The residence time of liquid in the reboiler is calculated using the inlet liquid flowrate, and the residence time of vapor in the condenser is calculated using the inlet vapor flowrate.

# 3 Model construction

We use a variant of the modeling scheme for polymer fouling in the distillation column presented in our previous work[6] to build the oxygen-perturbed fouling model. The model structure is the same as the base case model, while the liquid-phase and film-phase submodels are modified to accommodate the autoxidation chemistry.

The modeling scheme models the fouling in the distillation column as 40 interconnected tray models. Each tray model contains four submodels corresponding to different phases: the tray overhead vapor, tray bulk liquid, the liquid absorbed in the film, and the solid film growing on the tray surface. Each phase submodel is assumed to be perfectly homogeneous. The vapor phase submodel accounts for the vapor-liquid mass transfer, vapor-liquid equilibria, and the vapor convective flow from one tray to another. Due to the short residence time (Fig. 3(e)) and low concentration observed from the Aspen simulation, the vapor phase chemical reactions are assumed to be negligible. Details on the liquid-phase submodel and the film-phase submodel can be found in Sec. 3.1 and Sec. 3.3.

## 3.1 Liquid-phase submodel generation

The liquid-phase submodel accounts for the vapor-liquid mass transfer, vapor-liquid equilibria, liquid convective flow from one tray to another, and the liquid-phase oligomerization and autoxidation chemistry in the bulk tray liquid. The vapor-liquid mass transfer fluxes are modeled using two-film theory with liquid volumetric mass transfer coefficient ($k_{\text{liq}}A$) and Henry's law constant ($k_{\text{H}}$). $k_{\text{liq}}A$ is estimated using the temperature-dependent empirical correlation[24] derived from solvent viscosity, solvent density, and solute diffusion coefficients. These properties can either be found in the RMG-database,[17] or estimated by RMG using the CoolProp package.[25] $k_{\text{H}}$ is estimated using the temperature-dependent vapor-liquid equilibrium estimator[26] in RMG.

The detailed oligomerization and autoxidation mechanism for the liquid-phase submodel

is generated using Reaction Mechanism Generator (RMG). We seed the mechanism generation using the oligomerization mechanism in the base case debutanizer fouling model (without oxygen) for consistency. For the mechanism generation, we use 40 simulators, each corresponding to the tray liquid at each tray, condenser, and reboiler. We initialize these simulators using the temperatures, major species concentrations, volumetric flow rates, and dissolved oxygen concentrations at each tray, condenser, and reboiler in the debutanizer obtained from the Aspen simulation.

Most of the gas-phase thermochemistry is estimated by RMG using methods in RMG-database[15–18] or found in RMG-database. Some of the critical species are refined using quantum chemical calculations. Similarly, most of the rate coefficients are estimates by RMG using methods in RMG-database,[15–18] but some of the critical ones are refined using quantum chemical calculations. See Sec. 4 for the details on quantum chemistry calculations. Additionally, the distribution of sources of gas-phase thermochemistry and rate coefficients can be found in Fig. S5. Detailed comments regarding the sources of each thermochemical parameter and rate coefficient can be found in the mechanism files generated by RMG in our GitHub repository at `https://github.com/hwpang/PolymerFoulingModeling`.

Liquid-phase effects are accounted for as follows. The gas-phase thermochemistry is converted to the liquid-phase thermochemistry by applying the solvation energy corrections estimated using the method of Chung et al.[27] These corrections affect the reverse direction rates, which are calculated using the forward direction rates along with equilibrium constants computed from the solvation-corrected reaction Gibbs free energies. The solvation kinetic effects can also be important for the forward direction but are not considered in this work due to the lack of an accurate and robust estimator for solvation correction in reaction barrier heights. Diffusion-limited rates are applied based on the works of Rice et al.[28] and Flegg et al.[29]

## 3.2 Estimating heavy tail of oligomer distribution using Anderson-Schulz-Flory (ASF) method

To create a manageable oligomerization mechanism for simulation, species with a size greater than 16 heavy atoms are excluded. However, larger oligomers are formed in reality and may be significant in certain situations, making it unwise to completely neglect them. The Anderson-Schulz-Flory (ASF) distribution, which is based on ideal chain-growth polymerization, is utilized to estimate the number of large oligomers formed. The ASF theory predicts the mass fraction of chains with a length of $k$ monomers based on $\alpha$, the probability of chain elongation (Eq. 1). $\alpha$ can be calculated using the rate of production analysis (Eq. 2).

$$w(k) = \alpha^2 k(1-\alpha)^{k-1} \tag{1}$$

$$\alpha = \frac{r_\mathrm{p}}{r_\mathrm{p} + r_\mathrm{f} + r_\mathrm{t}} \tag{2}$$

where $r_\mathrm{p}$, $r_\mathrm{f}$, and $r_\mathrm{t}$ are the rates of chain propagation, chain transfer, and chain termination, respectively. In our system, there are several different molecular weight growth mechanisms. The definition of $\alpha$ corresponding to different types of polymer growth chemistry can be found in Sec. 5.1.

## 3.3 Film-phase submodel generation

The film-phase submodel accounts for the film growth chemistry on the tray surface. The film-phase submodel assumes an initial thin film of 10 $\mu$m on the tray surface due to imperfect cleaning. We assume that the tray liquid swells the film, so all the reactive sites on the film are in contact with the liquid-phase species absorbed in the film. The absorbed liquid-phase species reacts with the reactive site on the film to form covalent bonds to the film, resulting

in film growth chemically. As the film grows thicker, the film growth can become diffusion-limited, such that only the reactive sites near the surface of the film are in contact with sufficient amounts of absorbed reactive liquid-phase species to react, which would effectively cap the growth rate as the film thickens.

Since the film growth chemistry revolves around the reactive sites on the film, we represent the film growth chemistry using a variant of fragment-based modeling,[20] where the reactive sites on the film are lumped as reactive fragments participating in the liquid/solid interface reactions as reactants and/or products. In order to incorporate new types of reactive sites on film due to autoxidation chemistry, new fragments are defined. The reactive fragments considered in the oxygen-perturbed fouling model are the carbon-carbon double bond (CDB), the allylic hydrogen (AH), the allylic radical (AR), the alkyl radical (KR), the carbon peroxide (CP), the hydroperoxide (HP), the peroxyl radical (PR), and the alkoxyl radical (OR), as shown in Fig. 4.

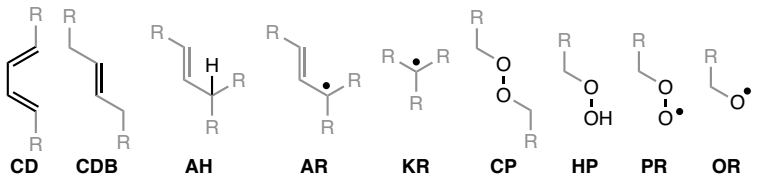


Figure 4: Fragments considered for the film-phase submodel. From left to right: conjugated diene (CD), carbon-carbon double bond (CDB), allylic hydrogen (AH), allylic radical (AR), alkyl radical (KR), carbon peroxide (CP), hydroperoxide (HP), peroxyl radical (PR), and alkoxyl radical (OR).

Additionally, new fragment-based reaction templates are defined to accommodate autoxidation reactions. The fragment-based reaction templates considered for the oxygen-perturbed fouling model are illustrated in Figs. S1 to S4. It includes several types of radical addition, several types of hydrogen atom abstraction, Diels-Alder addition (DA), ene reaction, peroxyl formation, hydroperoxyl concerted addition, and peroxide/hydroperoxide decomposition.

All exothermic reactions and hydrogen atom abstractions by KR and OR are regarded as irreversible, while other types of hydrogen atom abstraction and peroxide/hydroperoxide

decomposition are considered reversible. The irreversible assumption is an important simplification because the stoichiometric coefficients of the product side change when we break Product(S) into simpler fragments, and it doesn't make physical sense to use the fragment-based stoichiometric coefficients to compute the reverse rate directly. A more comprehensive procedure would be needed to correctly include the back reactions. The irreversible assumption is plausible in the distillation column temperature range. Note that the total creation/destruction of carbon center radicals (either allylic or radical radicals) by reactions within the thin film is negligible compared to the much larger radical creation/destruction rates in the much larger volume of bulk liquid, so the kinetics are not sensitive to these low-flux reactions in the film.

A representative structure is assigned to each fragment for estimating its thermochemistry using methods described in Sec. 3.1. Details on the generation of film growth mechanism based on reaction templates in Figs. S1 to S4 and the computation of fragment-based stoichiometric coefficients can be found in the SI of our prior work.[6]

The effects of the truncated liquid-phase oligomers on fouling growth are recovered using a fragment-based modeling approach.[20] We consider the reactions between the functional groups on the heavy tail of liquid-phase oligomers and the reactive site on the solid, instead of using the heavy-chain oligomers explicitly, to prevent an over-complicated model while maintaining interpretability. The steady-state concentration of the functional groups on the heavy tail of liquid-phase oligomers in each tray is estimated using $\alpha$ and $w(k)$, which is elaborated in Sec. S2.7.

## 3.4 Simulation of oxygen-perturbed debutanizer fouling model

The oxygen-perturbed debutanizer fouling model is a complex system consisting of multiple components. It encompasses 724 vapor-phase species, 724 bulk liquid-phase species, 22,383 liquid+liquid reactions in the bulk liquid, 724 liquid-phase species absorbed in the film, 8 types of reactive sites on the film, and 6,606 liquid+solid interface reactions for each tray.

Since the column has 40 trays, there are at least $(3 \times 724 + 8) \times 40 = 87{,}200$ state variables. When the spatial gradients in the films are considered, the number of state variables becomes even larger. The radicals in the system have a short chemical time scale, typically in the range of milliseconds. On the other hand, the residence time, representing the average time a species spends in the system, is tens of seconds at each tray. Furthermore, the overall simulation time span for the fouling model is extended to 1 year to capture long-term effects and assess the model performance over the extended period representative of industrial fouling time scales. The large number of state variables and large separation of time scales pose challenges in simulating the fouling model.

The governing equations for the tray vapor and tray liquid in tray $j$ are the same as those in our previous work,[6] as summarized below. Note that in this work, we use underscore for column vectors and boldface for matrices for clarity.

$$\frac{\mathrm{d}\underline{N}^j_{\mathrm{vap}}}{\mathrm{d}t} = \underline{\mathcal{T}}^j_{\mathrm{liq}\,\to\,\mathrm{vap}} + \underline{\mathcal{T}}^j_{\mathrm{vap}} + \cancelto{0}{\underline{\mathcal{R}}^j_{\mathrm{vap}}} \tag{3}$$

$$\frac{\mathrm{d}\underline{N}^j_{\mathrm{liq}}}{\mathrm{d}t} = -\underline{\mathcal{T}}^j_{\mathrm{liq}\,\to\,\mathrm{vap}} + \underline{\mathcal{T}}^j_{\mathrm{liq}} + \underline{\mathcal{R}}^j_{\mathrm{liq}} - \cancelto{0}{\underline{\mathcal{T}}^j_{\mathrm{liq}\,\to\,\mathrm{film}}} \tag{4}$$

$$\underline{\mathcal{T}}^j_{\mathrm{liq}\,\to\,\mathrm{vap}} = \underline{k}_{\mathrm{liq}} A \left( \underline{C}^j_{\mathrm{liq}} - \frac{\underline{C}^j_{\mathrm{vap}} \mathrm{R} T^j}{\underline{k}_{\mathrm{H}}} \right) V_{\mathrm{liq}} \tag{5}$$

$$\underline{\mathcal{T}}^j_{\mathrm{vap}} = \dot{V}^{j+1}_{\mathrm{vap,out}} \underline{C}^{j+1}_{\mathrm{vap}} - \dot{V}^j_{\mathrm{vap,out}} \underline{C}^j_{\mathrm{vap}} \tag{6}$$

$$\underline{\mathcal{T}}^j_{\mathrm{liq}} = \dot{V}^{j-1}_{\mathrm{liq,out}} \underline{C}^{j-1}_{\mathrm{liq}} - \dot{V}^j_{\mathrm{liq,out}} \underline{C}^j_{\mathrm{liq}} \tag{7}$$

$$\underline{\mathcal{R}}^j_{\mathrm{liq}} = V^j_{\mathrm{liq}} \mathbf{S}_{\mathrm{liq}} \underline{r}_{\mathrm{liq}} (\underline{C}^j_{\mathrm{liq}}; \underline{k}_{\mathrm{f,liq}}(T^j), \underline{K}_{\mathrm{eq,liq}}(T^j)) \tag{8}$$

where $\underline{N}^j_{\mathrm{vap/liq}}$ are the number of moles in the bulk liquid or vapor in the $j^{\mathrm{th}}$ tray of the distillation column. We call the condenser Tray 1 and the reboiler as Tray 40. $\dot{V}^j_{\mathrm{vap/liq,out}}$ are the vapor/liquid volumetric flowrate leaving the $j^{\mathrm{th}}$ tray, $\underline{C}^j_{\mathrm{vap/liq}}$ are concentrations in the bulk liquid or vapor in the $j^{\mathrm{th}}$ tray, $\underline{k}_{\mathrm{liq}} A$ are the effective rates of distillation/condensation of each species, $T^j$ is the temperature in the $j^{\mathrm{th}}$ tray, and $\underline{k}_{\mathrm{H}}$ are Henry's Law constants. $\mathbf{S}_{\mathrm{liq}}$

is the matrix of stoichiometric coefficients for liquid+liquid reactions, $\underline{r}_{\text{liq}}$ are the reaction rates, $V_{\text{liq}}$ is the volume of liquid in each tray. Here we assume all the trays are full, with a diameter of 2.5 m and a height of 0.3 m, *i.e.*, $V_{\text{liq}}^2 = V_{\text{liq}}^3 = ...V_{\text{liq}}^{39} = (2.5/2)^2 \times \pi \times 0.3 = 1.47\text{m}^3$. We assume the liquid volume in the condenser and the reboiler are the same, *i.e.*, $V_{\text{liq}}^1 = V_{\text{liq}}^{40} = 1.47\text{m}^3$.

As in our prior work,[6] we neglect reactions occurring in the vapor phase and the effects of the very slow film growth chemistry on the composition of the bulk liquid in each tray of the distillation column. We solve this tightly coupled vapor-liquid system of ordinary differential equations (ODEs) using a variant of Speth-Strang operator splitting iteratively solving,

$$\frac{\mathrm{d}\underline{N}_{\text{vap}}^j}{\mathrm{d}t} = \underline{\mathcal{T}}_{\text{liq}\,\rightarrow\,\text{vap}}^j + \underline{\mathcal{T}}_{\text{vap}}^j + \underline{q}_{n,\text{vap}}^j \tag{9}$$

$$\frac{\mathrm{d}\underline{N}_{\text{liq}}^j}{\mathrm{d}t} = -\underline{\mathcal{T}}_{\text{liq}\,\rightarrow\,\text{vap}}^j + \underline{\mathcal{T}}_{\text{liq}}^j + \underline{q}_{n,\text{liq}}^j \tag{10}$$

then solving

$$\frac{\mathrm{d}\underline{N}_{\text{vap}}^j}{\mathrm{d}t} = -\underline{q}_{n,\text{vap}}^j \tag{11}$$

$$\frac{\mathrm{d}\underline{N}_{\text{liq}}^j}{\mathrm{d}t} = \underline{\mathcal{R}}_{\text{liq}}^j - \underline{q}_{n,\text{liq}}^j \tag{12}$$

where the constants $\underline{q}_{n,\text{vap}}^j$ and $\underline{q}_{n,\text{liq}}^j$ for the $n^{\text{th}}$ time step are chosen to reduce the error in steady-state solution associated with operator splitting as discussed in Ref. 30 and in our previous work.[6] Note that the transport equations are decoupled in species, so the transport of each species can be solved separately. Also, the reaction equation is decoupled by trays. This keeps the number of equations small enough that we can use efficient stiff ODE solvers. For more details on the simulation scheme, see the SI and our previous work.[6]

The presence of oxygen significantly accelerates the film growth process, allowing the film to reach a considerable thickness. As the film grows thicker, the film growth rate transitions into a diffusion-limited regime. Consequently, our previous[6] assumption that the concentration of liquid-phase species absorbed in the film equals the concentration in the bulk liquid is no longer valid.

Specifically, the diffusion of dissolved oxygen from the bulk liquid into the film becomes a limiting factor in the growth process. This phenomenon can give rise to distinct regions with different dominating film growth pathways. To investigate these spatial effects on film growth chemistry, we consider axial ($z$) film growth, assuming the film is uniform in the other directions. There are many components to consider, as illustrated in Fig. 5. There are reactive sites on the solid in the film, participating in liquid+solid reactions to cause film growth. There are species in the liquid absorbed in the film, participating in both liquid+liquid reactions to cause chain initiation, propagation, and termination and liquid+solid reactions to cause film growth. The gradient in species concentration in the absorbed liquid causes diffusive fluxes. As the film grows, the interface between the bulk liquid and the film is moving and more liquid and liquid-phase species are absorbed into the film.

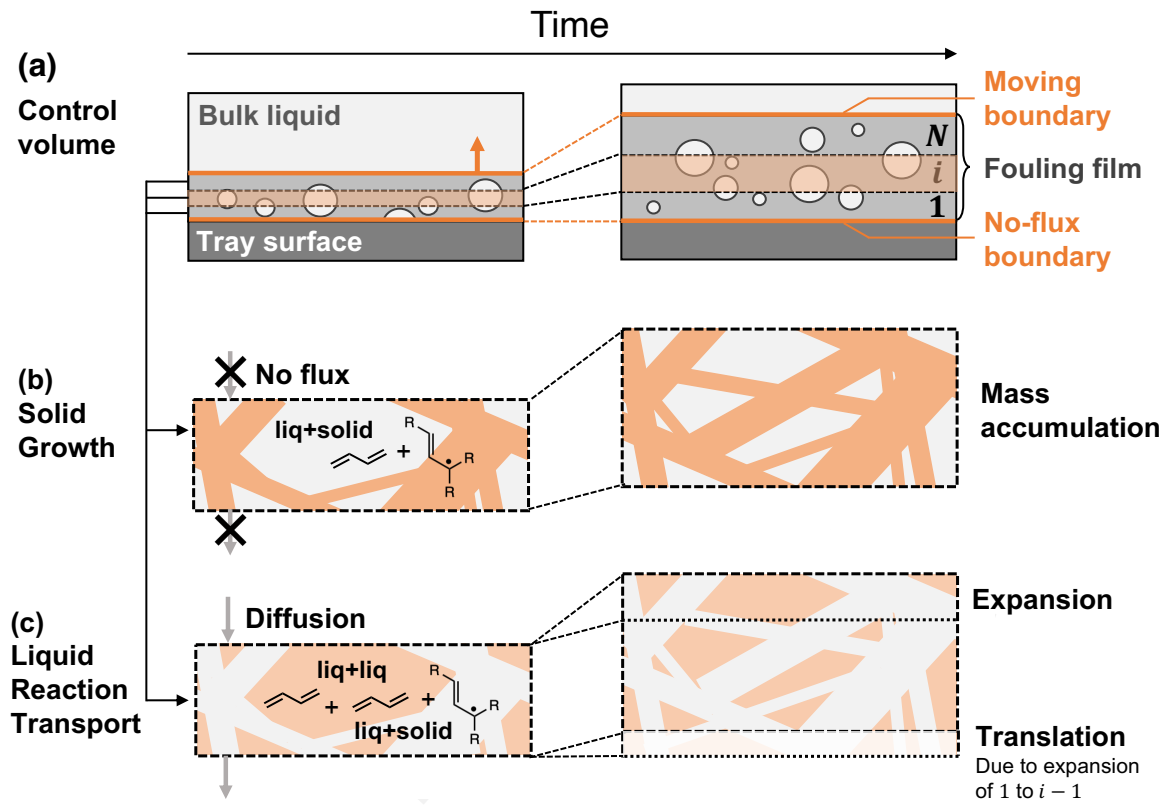


Figure 5: Components considered for one-dimensional film growth. The polymeric solid film has some liquid-filled pores and also some of the liquid dissolves into the solid.

We simulate the one-dimensional film growth using the finite volume method and discretize the film in the axial direction. We refer to the control volume at the boundary near the tray surface as $i = 1$ and the one near the bulk liquid as $i = N$, where $i$ is the index of each discretization, and $N$ is the total number of discretizations. For boundary conditions, we assume a no-flux boundary at the tray surface, and we assume the liquid-phase species concentrations in the bulk liquid stay at the steady-state concentrations, as illustrated in Fig. 5(a). In order to handle the moving boundary, we define the control volume such that it expands when the solid mass within it increases, and it moves in space when control volumes below it grow and push it toward the bulk liquid. We derive the governing equations starting from the macroscopic conservation equation for moving control volume,[31]

$$\frac{\mathrm{d}}{\mathrm{d}t}\int_{V(t)} C\mathrm{d}V = -\int_{S(t)} \overrightarrow{n}\cdot\overrightarrow{F}\mathrm{d}S + \int_{V(t)} \dot{\omega}(C)\mathrm{d}V + \int_{S(t)} \overrightarrow{n}\cdot\overrightarrow{F}_S\mathrm{d}S \tag{13}$$

where $C$ is the concentration, $V(t)$ is the time-dependent control volume, $S(t)$ is the time-dependent control surface, $\overrightarrow{n}$ is the outward unit normal vector, $\overrightarrow{F}$ is the diffusive flux, $\dot{\omega}$ is the rate of formation per unit volume, $\overrightarrow{F}_S$ is the flux caused by the moving control surface.

Below, we derive the governing equations for solid-bound reactive sites and liquid phase species absorbed in the film, respectively, starting from Eq. 13. Assuming reactive site concentrations within a control volume are homogeneous, we can integrate Eq. 13 for the solid part to obtain the governing equation for reactive sites in control volume $i$ of swollen film on tray $j$ (Eq. 14). We defne the control volume with respect to the solid-bound reactive sites and masses, such that all changes in solid-bound reactive sites and masses are due to liquid+solid reactions, as illustrated in Fig. 5(b).

$$\begin{aligned}
\frac{\mathrm{d}\underline{N}^{j,i}_{\mathrm{fragm}}}{\mathrm{d}t} &= \mathbf{S}_{\mathrm{liq+solid,fragm}}\underline{R}_{\mathrm{liq+solid}} \\
\underline{R}_{\mathrm{liq+solid}} &= \underline{R}_{\mathrm{liq+solid}}(\underline{N}^{j,i}_{\mathrm{fragm}}\underline{C}^{j,i}_{\mathrm{liq}\in\mathrm{film}}; \underline{k}_{\mathrm{f,liq+solid}}(T^j), \underline{K}_{\mathrm{eq,liq+solid}}(T^j))
\end{aligned} \tag{14}$$

where $\underline{N}^{j,i}_{\mathrm{fragm}}$ is the number of moles of reactive sites in control volume $i$ of swollen film on the surface of tray $j$, $\mathbf{S}_{\mathrm{liq+solid,fragm}}$ is the rectangular $8 \times 6{,}606$ stoichiometric matrix for reactive sites (the shape is the number of fragments by the number of liquid+solid reactions), $\underline{R}_{\mathrm{liq+solid}}$ are the rates of the liquid+solid reactions, $\underline{k}_{\mathrm{f,liq+solid}}$ and $\underline{K}_{\mathrm{eq,liq+solid}}$ are the rate constants and the equilibrium constants for the liquid+solid reactions (see the SI of our prior work 6 for the estimation of $\underline{K}_{\mathrm{eq,liq+solid}}$), and $\underline{C}^{j,i}_{\mathrm{liq}\in\mathrm{film}}$ are the concentrations of liquid-phase species absorbed in the film in control volume $i$ of swollen film on tray $j$.

We use the consumption of the liquid-phase species by liquid+solid reactions to track how much mass has been added to the solid part of the film. The corresponding governing equation for the mass of solid in control volume $i$ of tray $j$ ($m^{j,i}$) is

$$\frac{\mathrm{d}m^{j,i}}{\mathrm{d}t} = -\underline{M}_{\mathrm{w,liq}}^{\mathrm{T}}\mathbf{S}_{\mathrm{liq+solid,liq}}\underline{R}_{\mathrm{liq+solid}} \tag{15}$$

where $\mathbf{S}_{\mathrm{liq+solid,liq}}$ is the stoichiometric matrix for liquid-phase species absorbed in the film (with a shape of the number of liquid-phase species by the number of liquid+solid reactions), and $\underline{M}_{\mathrm{w,liq}}$ is the molecular weight of the liquid-phase species. The negative sign is because when a liquid-phase species gets consumed by a liquid+solid reaction to form a covalent bond with the solid, the mass of the solid increases.

Similarly, we can integrate Eq. 13 for the liquid part to obtain the governing equations for liquid-phase species absorbed in control volume $i$ of swollen film on the surface of tray $j$ (Eq. 16). As illustrated in Fig. 5(c), the number of moles of liquid-phase species in control volume $i$ of tray $j$ ($\underline{N}_{\mathrm{liq}\in\mathrm{film}}^{j,i}$) can change due to the diffusive flux entering/leaving the control volume $i$ at the top and bottom boundaries ($A\underline{F}_{\mathrm{liq}}$), liquid+liquid reactions ($\underline{\Omega}_{\mathrm{liq}}$), liquid+solid reactions ($\underline{\Omega}_{\mathrm{liq+solid}}$), translation of the control volume $i$ due to the expansion of control volumes below it, and expansion of the control volume $i$ due to mass accumulation.

$$\frac{\mathrm{d}\underline{N}_{\mathrm{liq}\in\mathrm{film}}^{j,i}}{\mathrm{d}t} = A\underline{F}_{\mathrm{liq}} + \underline{\Omega}_{\mathrm{liq}} + \underline{\Omega}_{\mathrm{liq+solid}} + \underbrace{\left(\sum_{k=1}^{i-1}\dot{V}_{\mathrm{liq}\in\mathrm{film}}^{j,k}\right)(\underline{C}_{\mathrm{liq}\in\mathrm{film}}^{j,i+1} - \underline{C}_{\mathrm{liq}\in\mathrm{film}}^{j,i})}_{\text{translation}} + \underbrace{\dot{V}_{\mathrm{liq}\in\mathrm{film}}^{j,i}\underline{C}_{\mathrm{liq}\in\mathrm{film}}^{j,i+1}}_{\text{expansion}} \tag{16}$$

$$\underline{F}_{\mathrm{liq}} = \underline{D}_{\mathrm{liq}}\left.\frac{\partial \underline{C}_{\mathrm{liq}\in\mathrm{film}}^{j,i}}{\partial z}\right|_{i+1/2} - \underline{D}_{\mathrm{liq}}\left.\frac{\partial \underline{C}_{\mathrm{liq}\in\mathrm{film}}^{j,i}}{\partial z}\right|_{i-1/2} \tag{17}$$

$$\underline{\Omega}_{\mathrm{liq}} = \mathbf{S}_{\mathrm{liq}}\underline{R}_{\mathrm{liq}}(\underline{C}_{\mathrm{liq}\in\mathrm{film}}^{j,i}, V_{\mathrm{liq}\in\mathrm{film}}^{j,i}; \underline{k}_{\mathrm{f,liq}}, \underline{K}_{\mathrm{eq,liq}}) \tag{18}$$

$$\underline{\Omega}_{\mathrm{liq+solid}} = \mathbf{S}_{\mathrm{liq+solid,liq}}\underline{R}_{\mathrm{liq+solid}} \tag{19}$$

where $\underline{C}^{j,i}_{\text{liq}\in\text{film}}$ refers to the concentration of liquid-phase species in control volume $i$, and $\underline{C}^{j,N+1}_{\text{liq}\in\text{film}} = \underline{C}^{j}_{\text{liq,S.S.}}$. $\underline{D}_{\text{liq}}$ is the diffusion coefficient for liquid-phase species, $i \pm 1/2$ refers to the top/bottom boundary of the control volume $i$, $V^{j,i}_{\text{liq}\in\text{film}}$ is the volume of liquid part in control volume $i$, $\dot{V}^{j,i}_{\text{liq}\in\text{film}}$ is the rate of change for the volume of liquid part in control volume $i$. $V^{j,i}_{\text{liq}\in\text{film}}$ and $\dot{V}^{j,i}_{\text{liq}\in\text{film}}$ are computed using

$$V^{j,i}_{\text{liq}\in\text{film}} = \Delta z^{j,i} A \epsilon \tag{20}$$

$$\dot{V}^{j,i}_{\text{liq}\in\text{film}} = \Delta \dot{z}^{j,i} A \epsilon \tag{21}$$

Note that the size of a control volume $i$ ($\Delta z^{j,i}$) and rate of change in the size of a control volume $i$ ($\Delta \dot{z}^{j,i}$) is obtained by

$$\Delta z^{j,i} = \frac{m^{j,i}}{\rho_{\text{solid}}} \frac{1}{1-\epsilon} \frac{1}{A} \tag{22}$$

$$\Delta \dot{z}^{j,i} = \frac{\mathrm{d}m^{j,i}}{\mathrm{d}t} \frac{1}{\rho_{\text{solid}}} \frac{1}{1-\epsilon} \frac{1}{A} \tag{23}$$

where $\rho_{\text{solid}}$ is the density of the solid part, $\epsilon$ is the fraction of liquid in film by volume, and $A$ is the cross-sectional area of tray surface.

We approximate the first-order derivative at the control volume boundary using central difference,

$$\left.\frac{\partial \underline{C}^{j,i}_{\text{liq}\in\text{film}}}{\partial z}\right|_{i+1/2} = \begin{cases} \dfrac{\underline{C}^{j,i+1}_{\text{liq}\in\text{film}} - \underline{C}^{j,i}_{\text{liq}\in\text{film}}}{\frac{\Delta z^{j,i+1}}{2} + \frac{\Delta z^{j,i}}{2}} & \forall i \in \{1, ..., N-1\} \\ \dfrac{\underline{C}^{j}_{\text{liq, S.S.}} - \underline{C}^{j,i}_{\text{liq}\in\text{film}}}{\Delta z^{j,i}} & i = N \end{cases} \tag{24}$$

$$\left.\frac{\partial \underline{C}^{j,i}_{\text{liq}\in\text{film}}}{\partial z}\right|_{i-1/2} = \begin{cases} \dfrac{\underline{C}^{j,i}_{\text{liq}\in\text{film}} - \underline{C}^{j,i-1}_{\text{liq}\in\text{film}}}{\frac{\Delta z^{j,i}}{2} + \frac{\Delta z^{j,i-1}}{2}} & \forall i \in \{2, ..., N\} \\ 0 & i = 1 \end{cases} \tag{25}$$

Details on how we decide the number of discretizations ($N$) and other numerical simulation details can be found in Sec. S2.6.

# 4 Thermochemical and kinetic parameters from quantum chemistry calculations

We use quantum chemistry, statistical mechanics, and rate theory calculations to refine the thermochemical and kinetic parameters used in the chemical kinetic mechanisms of this study.

We employ the ARC software package[32] to automate parameter calculations. Starting with 2D representations of molecules, ARC uses RDKit[33] for generating 3D conformers, with a torsional mapping algorithm employed to identify the most energetically favorable conformers. Transition states (TSs) are input manually with initial 3D guess geometries. Quantum chemistry packages such as Gaussian 09[34] and 16[35] are then coordinated by ARC to optimize the geometry, calculate single-point energies, and determine harmonic frequencies. Rotor scans are performed for structures with hindered rotors. ARC also includes error handling and troubleshooting capabilities, automatically relaunching calculations with updated arguments if common errors or failures occur. The results obtained from the quantum calculations are collected and fed into Arkane,[15–18] a statistical mechanics and rate theory calculation package, to obtain thermochemical properties and reaction rate coefficients.

The CBS-QB3 level of theory[36] is chosen due to its favorable balance between computational cost and accuracy for predicting the properties of hydrocarbons. Within the CBS-QB3 calculation, geometry optimization and frequency calculations are performed at the B3LYP/CBSB7 level of theory. For rotor scans, constrained optimizations at the B3LYP/CBSB7 level are conducted on a 1D mesh with 45 evenly spaced points over a 360-degree rotation to obtain 1-D hindered rotor potentials. The partition functions of molecules and TSs are computed using the single conformer rigid rotor harmonic oscillator (RRHO) approximation,

with the corrections for 1D separable hindered rotors. To obtain rate coefficients, Transition State Theory (TST) with the Eckart tunneling correction is applied. Using this method, we anticipate an uncertainty of 1-2 kcal/mol in the standard enthalpy of formation[37] and an uncertainty of 2-3 kcal/mol in the barrier heights.[37] Using 2.5 kcal/mol as a representative value, this can correspond to a factor of $\exp^{\frac{2.5\times1000\times4.18}{8.314\times376.5}} \sim \exp^{\frac{2.5\times1000\times4.18}{8.314\times312.5}} = 30 \sim 50$ uncertainty in the predicted thickness, depending on the temperature (and thus the location in the column).

# 5 Results and discussion

## 5.1 Effects of dissolved oxygen on oligomerization in tray liquid

Film growth on the tray surface can arise from either non-radical or radical pathways. The main non-radical pathways are Diels-Alder addition reactions involving the monomers in the liquid absorbed in the film and the reactive sites on the solid, while the main radical pathways include the propagation of liquid-phase radicals with solid-bound double bonds, or solid-bound radicals with liquid-phase monomers.

For non-radical pathways, the influence of $O_2$ is marginal, as the concentration of monomers in the absorbed liquid remains similar to that in the bulk liquid, which predominantly depends on the convective flows, similar to the previously published base case (zero oxygen) scenario.[6] However, for radical pathways, $O_2$ has a much larger impact because the concentration of participating radicals in the absorbed liquid is primarily governed by diffusive fluxes and liquid+liquid reactions. The liquid+liquid reactions affecting the radical concentrations in the bulk liquid include both oligomerization and autoxidation.

Radicals in the bulk liquid can originate via inter-tray convective flow, vapor-liquid mass transfer, or they can be generated via chain initiation reactions, as shown in Fig. 6(d). The relative significance of these sources varies with location within the distillation column. In hotter regions with low dissolved oxygen concentrations, such as the reboiler and trays near

it, the dominant source of radicals remains consistent with the base case scenario studied in our previous work:[6] reverse disproportionation reactions between species with loosely bonded hydrogens (allylic hydrogens and bisallylic hydrogens) and conjugated dienes produce allylic radicals and bisallylic radicals, maintaining a relatively high radical concentration, as shown in Fig. 6(a) and (d). Many of these radicals have low molecular weight, and the elevated temperature in the reboiler facilitates their evaporation. They are carried upward by the convective flow of vapor to the condenser, where the temperature is low enough that they condense back into the liquid.

In the condenser and trays closer to the condenser, the dissolved oxygen concentration is relatively high. As a result, carbon-center radicals in these regions (mostly sourced from condensation) rapidly react with oxygen, transforming into peroxyl radicals, as shown in Fig. 6(c). Through hydrogen atom abstraction or recombination reactions, these peroxyl radicals can further convert into hydroperoxides or peroxides. The downward liquid convective flow transports these hydroperoxides and peroxides to the bottom section of the column. In this region, where the temperature is comparatively higher, a fraction of the hydroperoxides and peroxides decompose, turning into peroxyl and alkoxyl radicals and becoming the source of trace oxygen compound contamination despite negligible dissolved molecular oxygen, as shown in Fig. 6(a). In all trays, the radical reaction timescales are shorter than the residence time, so most radicals react. However, radical slows into and out of trays are often significant relative to the slow net radical formation reactions.

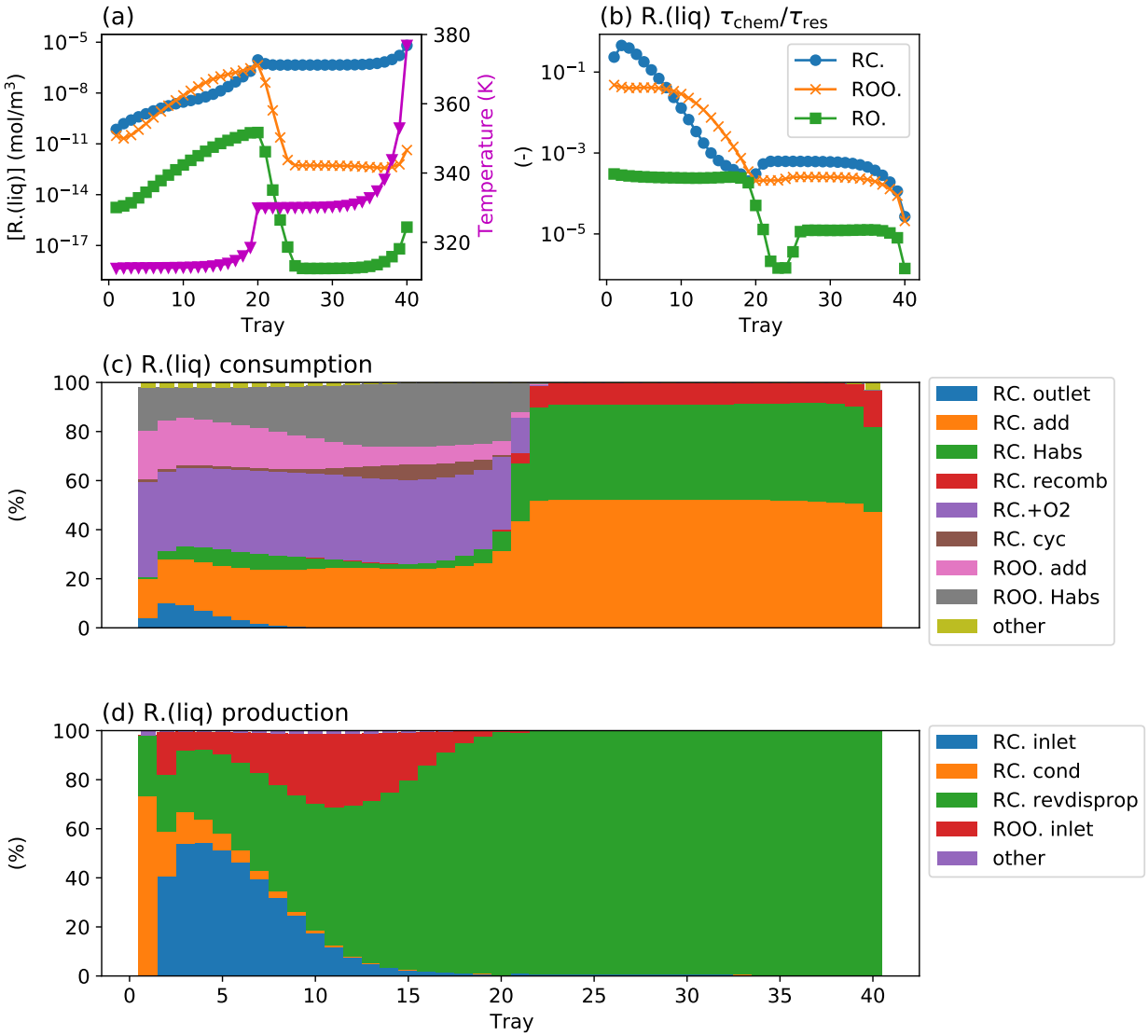


Figure 6: Radical concentration (a), radical chemical lifetime to residence time ratio (b), normalized radical consumption fluxes via various pathways (c), and normalized radical production fluxes via various pathways (d) in bulk liquid at each tray. RC., ROO., and RO. refer to carbon-center radicals, peroxyl radicals, and alkoxyl radicals.

In the liquid-phase system, in addition to the Diels-Alder (DA) polymerization and radical polymerization in the base case scenario,[6] the presence of dissolved oxygen gives rise to alkylperoxyl propagation chain, as illustrated in Fig. 7.

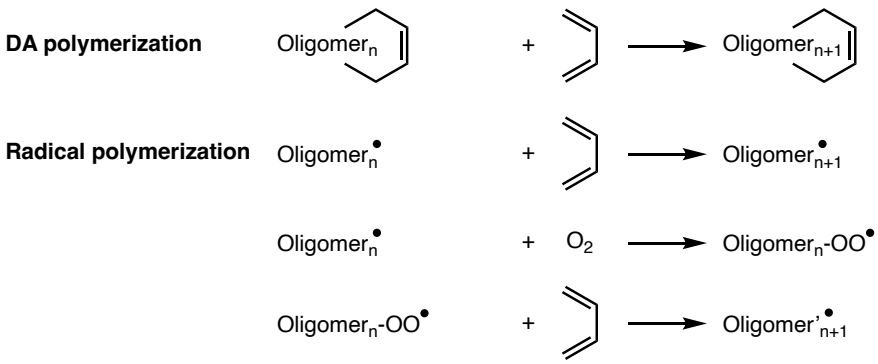


Figure 7: Patterns of possible polymerization pathways in the liquid-phase system with the presence of oxygen. For conciseness, the illustration omits the substituent groups of the monomers. For radical polymerization, monomers can be non-conjugated alkenes as well as dienes. The growing chain can either be alkyl or alkylperoxyl.

For DA polymerization, the elongation probability of an oligomer was found to be negligible in our previous work. For radical polymerization, the elongation probability depends on various types of radical consumption rates, fluxes, and reactions. The equation approximating the elongation probability for carbon-center growing chains ($\alpha_{\mathrm{RC.}}$), accounting for the effects of dissolved oxygen and oxygen chemistry, is as follows:

$$
\begin{aligned}
\alpha_{\mathrm{RC.}} &= \frac{r_{\mathrm{RC.,p}}}{r_{\mathrm{RC.,p}} + r_{\mathrm{RC.,f}} + r_{\mathrm{RC.,t}}} \\
r_{\mathrm{RC.,p}} &= r_{\mathrm{RC.\ add}} + r_{\mathrm{RC.}+O_2} \\
r_{\mathrm{RC.,f}} &= r_{\mathrm{RC.\ Habs}} \\
r_{\mathrm{RC.,t}} &= r_{\mathrm{RC.\ recomb}} + r_{\mathrm{RC.\ disprop}} + r_{\mathrm{RC.\ cyc}} + F_{\mathrm{out,\ RC.}} + F_{\mathrm{evap,\ RC.}}
\end{aligned}
\tag{26}
$$

where $r_{\mathrm{RC.}}$ stands for the flux of carbon-center radical consumption by a certain reaction type in moles per second, indicated by its subscript (radical addition 'RC. add'; hydrogen atom abstraction 'RC. Habs'; radical recombination 'RC. recomb'; radical disproportionation 'RC. disprop'; combination with oxygen 'RC.+$O_2$'; cyclic ether formation 'RC. cyc'), $F_{\mathrm{out,\ RC.}}$ is the flux of carbon-center radicals leaving via the liquid outlet flow, and $F_{\mathrm{evap,\ RC.}}$ is the evaporation flux of carbon-center radicals. Note that hydrogen atom abstraction terminates

the growing chain and initiates a new chain.

Carbon-center growing chains have the potential to combine with oxygen, converting them into peroxyl growing chains. The elongation probability for peroxyl growing chains ($\alpha_{\mathrm{ROO.}}$) can be approximated as follows:

$$\begin{aligned}
\alpha_{\mathrm{ROO.}} &= \frac{r_{\mathrm{ROO.,p}}}{r_{\mathrm{ROO.,p}} + r_{\mathrm{ROO.,f}} + r_{\mathrm{ROO.,t}}} \\
r_{\mathrm{ROO.,p}} &= r_{\mathrm{ROO.\ add}} \\
r_{\mathrm{ROO.,f}} &= r_{\mathrm{ROO.\ Habs}} \\
r_{\mathrm{ROO.,t}} &= r_{\mathrm{ROO.\ recomb}} + r_{\mathrm{ROO.\ disprop}} + r_{\mathrm{ROO.\ eli}} + F_{\mathrm{out,\ ROO.}} + F_{\mathrm{evap,\ ROO.}}
\end{aligned} \tag{27}$$

where $r_{\mathrm{ROO.}}$ stands for the peroxyl radical consumption flux by a certain reaction type in moles per second, indicated by its subscript (radical addition 'ROO. add'; hydrogen atom abstraction 'ROO. Habs'; radical recombination 'ROO. recomb'; radical disproportionation 'ROO. disprop'; concerted $HO_2$ elimination from peroxyl radical 'ROO. eli'), $F_{\mathrm{out,\ ROO.}}$ is the total out flux of peroxyl radicals, and $F_{\mathrm{evap,\ ROO.}}$ is the total evaporation flux of peroxyl radicals.

A peroxyl growing chain can revert to a carbon-center chain by adding to a double bond in a monomer. Considering the interconnected pathways for chain growth, it is reasonable to define an overall elongation probability for radical polymerization ($\alpha_{\mathrm{R.}}$) as follows:

$$\alpha_{\mathrm{R.}} = \alpha_{\mathrm{RC.}} \left(1 - (1 - \alpha_{\mathrm{ROO.}}) \frac{r_{\mathrm{RC.}+O_2}}{r_{\mathrm{RC.\ add}} + r_{\mathrm{RC.}+O_2}}\right) \tag{28}$$

where $\frac{r_{\mathrm{RC.}+O_2}}{r_{\mathrm{RC.\ add}}+r_{\mathrm{RC.}+O_2}}$ represents the probability of a carbon-center growing chain transitioning into an oxygen-center growing chain during elongation, while $1 - \alpha_{\mathrm{ROO.}}$ represents the probability of an oxygen-center growing chain not elongating.

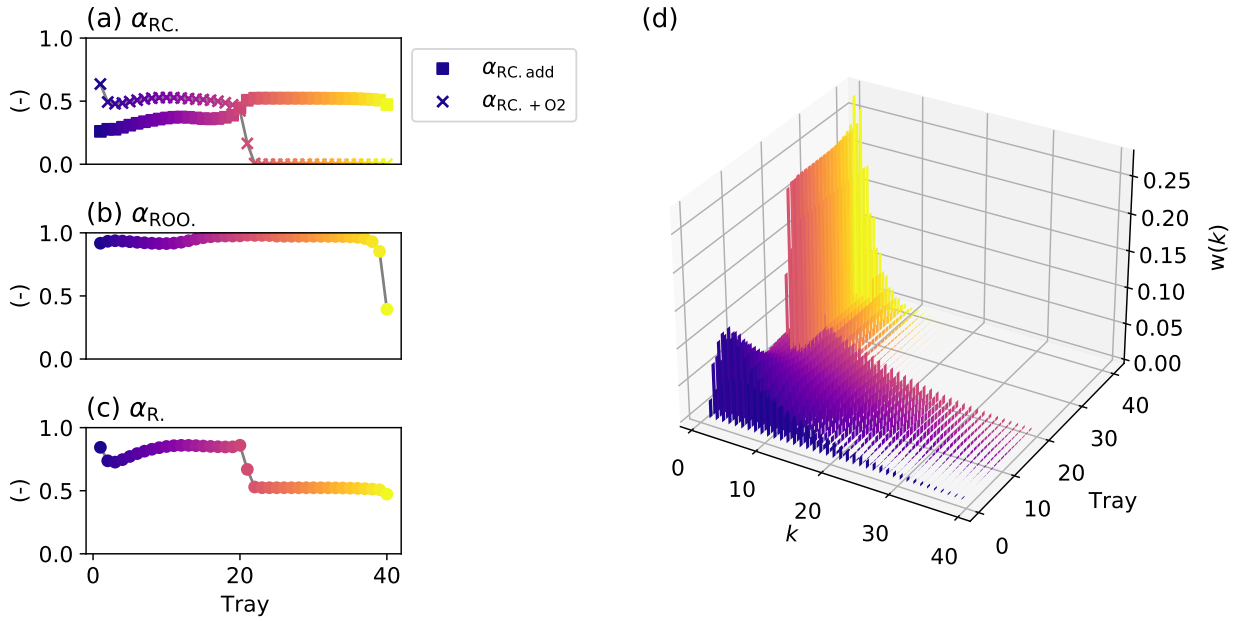


Figure 8: The chain elongation probability $\alpha$ across trays for carbon-center radicals only (a), peroxyl radicals only (b), the overall probability an oligomer chain grows (c), and the ASF distribution ($w(k)$) for the radical polymerization (d).

Fig. 8 (a) to (d) show the computed values of $\alpha_{\mathrm{RC.}}, \alpha_{\mathrm{ROO.}}, \alpha_{\mathrm{R.}}$, and the corresponding ASF distribution for $\alpha_{\mathrm{R.}}$ in the liquid-phase system. In Fig. 8 (a), $\alpha_{\mathrm{RC.}}$ is represented by two components: the elongation probability through monomer addition ($\alpha_{\mathrm{RC.\ add}}$) and the elongation probability by combining with dissolved oxygen to form an oxygen-center propagation chain. It can be observed that in the colder section, where the oxygen concentration is relatively higher, the carbon-center propagation chains have a greater likelihood of elongating by combining with dissolved oxygen (Fig. 8(a)). This transformation leads to the formation of peroxyl propagation chains with higher elongation probabilities (Fig. 8(b)). Consequently, the overall elongation probability for radical polymerization is relatively high in the colder section where oxygen is present (Fig. 8(c)).

The ASF distribution, shown in Fig. 8(d), demonstrates that the presence of oxygen allows for the growth of larger and heavier oligomers. These oligomers may become heavy enough to physically deposit onto the tray surface if their concentration gets high enough, but the film growth attributed to monomer-involving pathways still dominates, so we did

not attempt to model that process.

Sensitivities of chain elongation probability shown in Figs. 8 to different dissolved oxygen concentrations can be found in Fig. S13. The elongation probability of carbon-center radicals turning into peroxyl radicals increases as the dissolved oxygen concentration increases for the colder trays. These peroxyl propagation chains have a larger probability to add to monomers compared to the carbon-center radicals, leading to the increase in the overall elongation.

## 5.2 Effects of dissolved oxygen on film growth

Reactions forming covalent bonds between liquid-phase species absorbed in the film and reactive sites on the solid part of the film result in film growth. Understanding the key chemical reactions contributing to film growth is crucial for developing effective mitigation strategies. Film growth can occur through both non-radical and radical pathways. In our previous work,[6] we demonstrated the significant role of radical pathways in the base case where no oxygen was present.

In this section, we investigate the major liquid+solid reactions that contribute to film growth in the presence of air-saturated dissolved oxygen. We analyze one-dimensional film growth simulation snapshots over a one-year period. Our goal is to gain insights into the impact of oxygen on film growth and explore potential strategies to mitigate fouling in the debutanizer system.

Fig. 9 shows the film thickness as a function of time at selected trays. The film thickness increases exponentially in the early times. As the film gets thicker, it becomes diffusion-limited and transitions to linear growth. The film can grow up to $\mathcal{O}$(10cm). Note that this model assumes a weir height of 30 cm and a 60 cm of tray separation. As the film thickness approaches the weir height, the debutanizer can experience flooding and other physical phenomena that affect fouling growth.

Fig. 10 shows the rate of film growth through important reactions at selected trays at the initial time and 1 year. The dominating film growth chemistry changes over time. With

the higher concentration of dissolved oxygen in the colder section of the debutanizer, the film growth is initially dominated by oxygen-driven fast-growth pathways.

There are two possible pathways in which dissolved oxygen can accelerate film growth in the cold section. The first one is through the solid-bound radical pathways. Under an anaerobic condition, there are two types of solid-bound radical reactive sites: the allylic radical reactive site (AR) and the alkyl radical reactive site (KR). With dissolved oxygen, there is enough dissolved oxygen within the film initially. Some of these carbon-center solid-bound radicals rapidly combine with an oxygen molecule and convert into peroxyl radical reactive site (PR). All of these solid-bound radicals can convert to one another through propagation reactions with conjugated diene monomers. The monomer concentrations within the film stay similar to those in the bulk liquid. The relatively high concentration of dissolved oxygen and less availability of loosely bonded allylic hydrogens in the colder trays (since the dominant species, butadiene, does not have any very weak C−H bonds) generally promote this film growth cycle. However, our quantum calculations show that PR propagates with conjugated diene monomers at similar $k$'s to AR (Fig. S14). Additionally, the rate of production analysis shows that the amount of growth caused by a PR (Fig. S16) is similar to that of AR (Fig. S15). Considering these, the fast growth caused by dissolved oxygen is not through the solid-bound radical pathways.

The second one is through the liquid-phase radical pathways. Both the liquid-phase carbon-center and oxygen-center (mostly peroxyl) radicals react with solid-bound carbon-carbon double-bond reactive sites (CDB) to cause film growth. There are few solid-bound conjugated diene reactive sites (CD) as they are brought in by the slow propagation of bisallylic radicals, so the propagation of liquid-phase radicals with CD is not significant. Our quantum calculations show that these peroxyl radicals react with CDB at a much faster rate (ranging from 1 to 3 orders of magnitude depending on the radical structure, as shown in Fig. S14) compared to their corresponding allylic radicals. The rate of production analysis shows that the amount of growth caused by a liquid-phase oxygen-center radical (Fig. S18)

is several orders of magnitude more than that by a liquid-phase carbon-center radical (Fig. S17). Moreover, due to the reason explained in Sec. 5.1, under an aerobic condition, many of these liquid-phase radicals are relatively large and have many carbon-carbon double bonds and peroxides on their backbone. This suggests that peroxyl radicals also bring in more reactive sites onto the film as they react. In short, the dissolved oxygen accelerates the film growth through the liquid-phase radical pathways, by making the liquid-phase radicals more reactive towards the solid.

As the film grows thicker, the diffusion of dissolved oxygen from the bulk liquid into the film becomes a controlling factor in the growth process. This gives rise to two distinct regions within the film, as illustrated in Fig. 11. One is the oxygen-driven fast growth region, located near the tray surface where the concentration of dissolved oxygen is sufficiently high, thereby enabling fast oxygen-involved film growth pathways to prevail. The other region is characterized by slower anaerobic growth similar to the situation studied in the previous work.[6]

Due to the low concentration of dissolved oxygen in the hotter section of the distillation column, film growth is initially governed by carbon-center radical pathways. As the film grows thicker, the flow of radicals from the bulk into the film becomes diffusion-limited, causing the accumulation of solid-bound radical reactive sites to decrease. Note that the loss of solid-bound radical reactive sites is not affected by film thickness, because the dominant consumption pathways of solid-bound radical reactive sites are via the hydrogen atom abstraction with a loosely bounded hydrogen on a monomer, while the monomer concentration in the film remains about the bulk liquid and is not limited by diffusion. Consequently, the film growth via the Diels-Alder pathways is not affected by diffusion and thus becomes competitive with the carbon-center radical pathways. In the reboiler, the elevated temperature and the higher concentration of cyclopentadiene cause the Diels-Alder pathways to dominate even at early times.

This suggests that additives such as antioxidants applied in the colder section of the

debutanizer have the potential to mitigate film growth at early times, while inhibitors targeting ordinary radical polymerization may be required at a later stage. Inhibitors targeting ordinary radical polymerization may be required in the hotter section of the debutanizer.

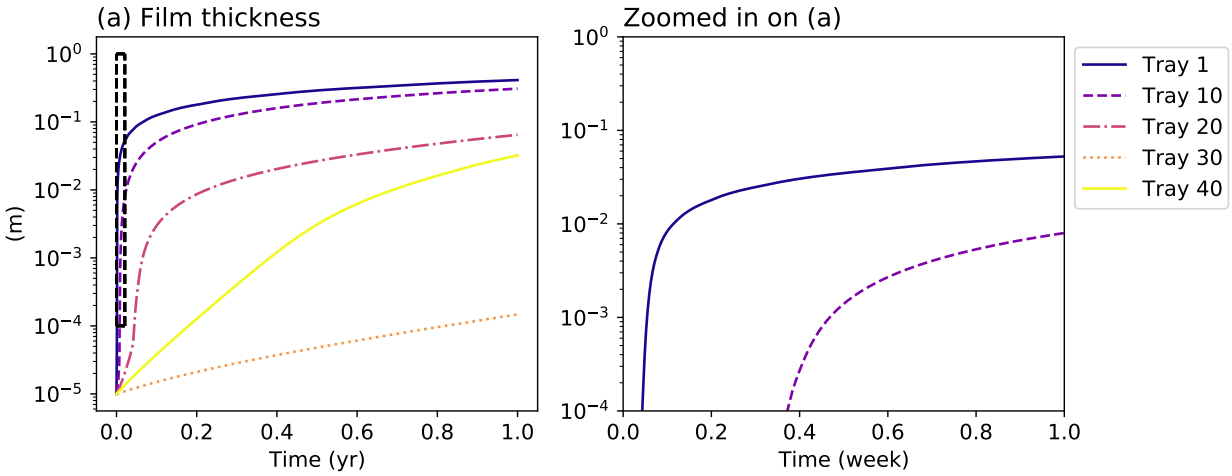


Figure 9: Predicted fouling film thickness as a function of time at selected trays for cases where the feed (liquid entering at tray 20) is air-saturated with dissolved oxygen. When the films get thick, the growth slows because of diffusion limits.

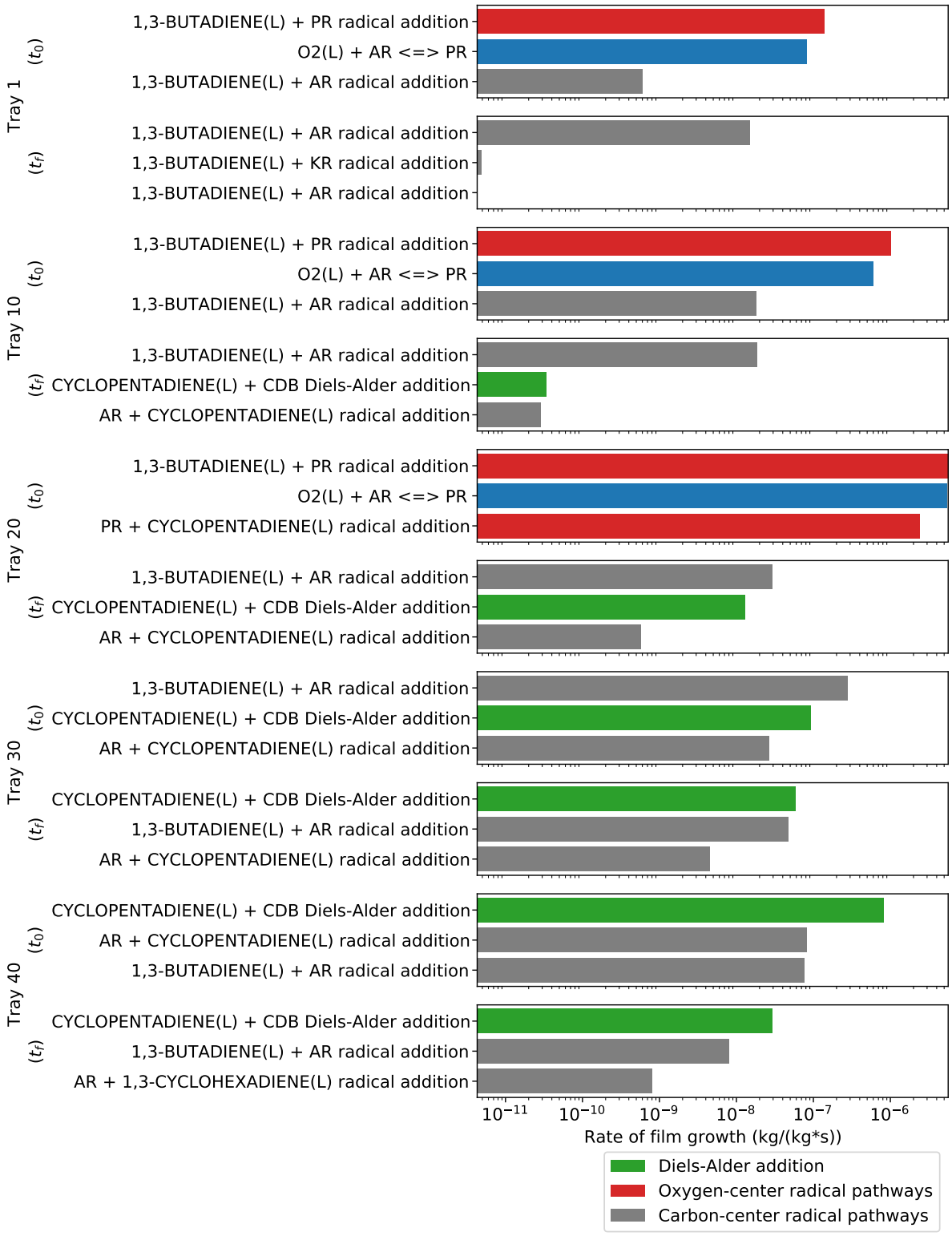


Figure 10: Rate of film growth by important reactions at selected trays at the initial time ($t_0$) and 1 year ($t_f$) in log scale. The rate of film growth refers to the rate of change in the solid mass by chemical pathways, summed across the film and normalized by the total solid mass. The most important reactive sites in the film are peroxyl radicals (PR), allylic radicals (AR), ordinary radicals (KR), and carbon double bonds (CDB).

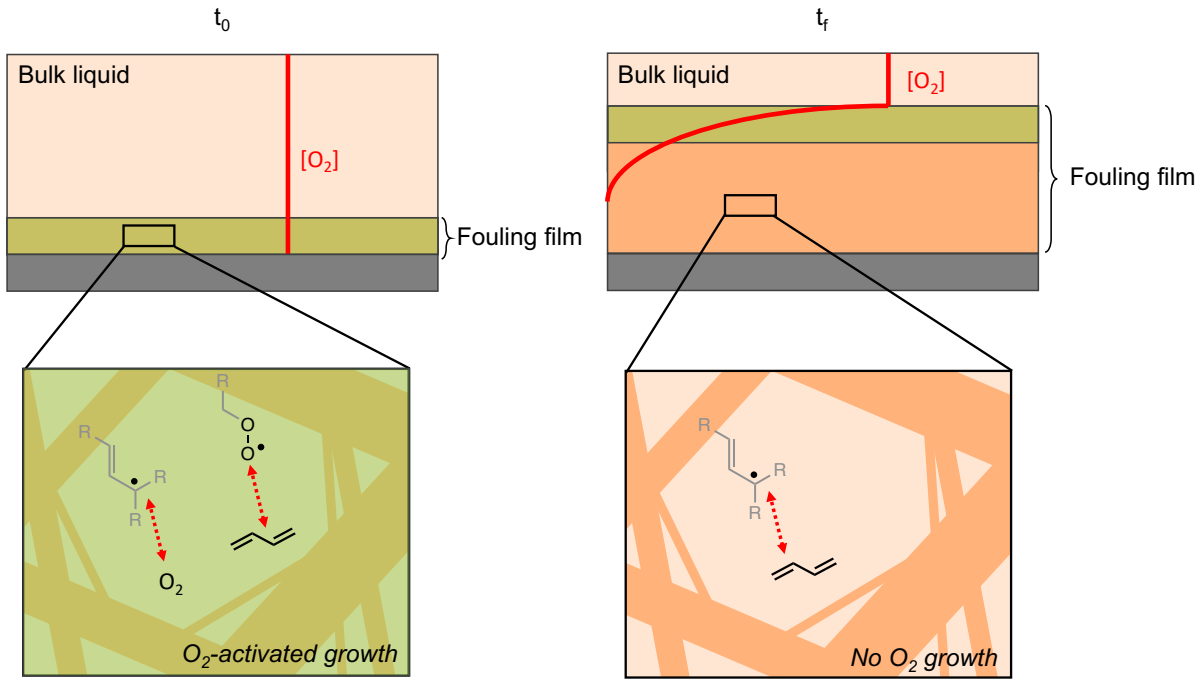


Figure 11: Illustration of diffusion-limited film growth when oxygen is present in the bulk liquid at the initial time ($t_0$) and 1 year ($t_f$). As dissolved oxygen is quickly consumed, two film growth regions are created: an oxygen-activated growth region near the tray surface, and an anaerobic growth region with depleted oxygen.

## 5.3 Sensitivity of fouling growth rates to concentrations of dissolved oxygen in feedstock

There are many possible sources of dissolved oxygen and oxygenates in a steam-cracking plant. Traces of dissolved oxygen can enter a distillation column along with the feedstock or the water used for quenching or any additives. The concentration of dissolved oxygen in the feedstock of the distillation column plays a significant role in the fouling growth rate. To investigate this sensitivity, we sample the dissolved oxygen concentration in the feedstock by a factor to its saturated concentration: 1 (feedstock contains saturated oxygen), $10^{-1}$, $10^{-2}$, $10^{-3}$ (parts per million level), $10^{-4}$, $10^{-5}$, $10^{-6}$ (parts per billion level), and 0 (no oxygen in the feedstock). The system is simulated for 1 year (representative industrial fouling

timescale). The results of this sensitivity study are shown in Fig. 12.

When there is no dissolved oxygen present in the feedstock, the fouling growth rate is extremely slow, with a film thickness of micrometers to millimeters for most trays in 1 year, consistent with our finding in the base case study.[6] However, even a concentration as low as parts per million (ppm) of dissolved oxygen can significantly accelerate film growth to centimeters in 1 year. The impacts of dissolved oxygen in the feedstock center on the colder section of the debutanizer. This suggests that the boiling point of the antioxidant is a key design parameter to maximize the contact of the antioxidant and locations most affected by the molecular oxygen contamination, and that one may improve the effectiveness of antioxidant-type additives by introducing them from the condenser.

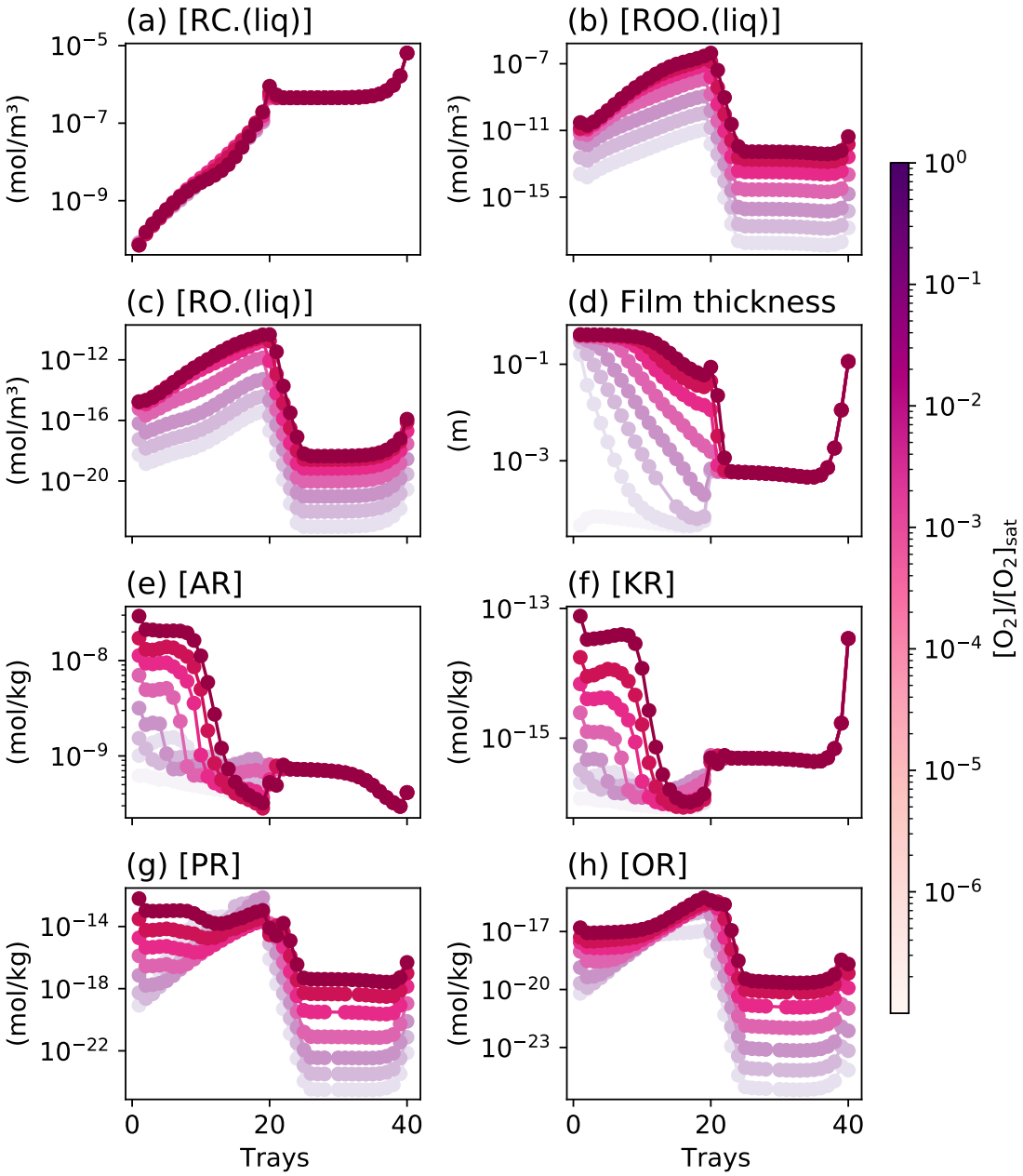


Figure 12: Sensitivity of carbon-center radical concentration in bulk liquid (a), peroxyl radical concentration in bulk liquid (b), alkoxyl radical concentration in bulk liquid (c), film thickness (d), allylic radical reactive site to solid mass ratio (e), ordinary radical reactive site to solid mass ratio (f), peroxyl radical reactive site to solid mass ratio (g), and alkoxyl radical reactive site to solid mass ratio (e) to different levels of dissolved oxygen in the feedstock to the debutanizer ($[O_2]_{sat}$ is air-saturated). All values are at $t = 1$ year.

# 6 Conclusions

This study presented a comprehensive extension of the multiphase detailed chemical kinetic modeling approach to incorporate the effects of dissolved oxygen in the context of polymer fouling within a distillation column. The fouling model specifically focused on the debutanizer and considered the presence of dissolved oxygen in the feedstock as the primary oxygen source. By explicitly accounting for 4 phases in each tray - tray overhead vapor, tray bulk liquid, liquid absorbed in the fouling film, and the solid in the fouling film on the tray surface - we constructed a detailed representation of the fouling process on the surface of a tray for 40 trays in a distillation column. The oxygen-perturbed polymerization occurring in the tray liquid was modeled using a detailed chemical mechanism. To manage the large number of distinct chemical species involved in the real fouling system, the molecular weight distribution of the oligomers formed in the bulk liquid was represented using the Anderson-Schulz-Flory (ASF) distribution to recover associated film growth contribution. Additionally, a fragment-based modeling approach was employed to describe the film growth chemistry, where the fragment-based reaction templates were modified to incorporate oxygen-perturbed film growth pathways.

Analyses on ASF distribution showed that heavy tails of oligomers can be formed via radical polymerization at the colder section of the column with the presence of oxygen, due to the larger elongation probability of the peroxyl propagation chain. We analyzed the simulation using rate of production analyses, and found that oxygen chemistry predominantly impacts liquid-phase radical polymerization and film growth in the colder section of the column. This is because the $O_2$ rises in the column and has a very low concentration in the hotter trays. We also found that the dominating film growth pathways can change at early and later fouling stages because thick films limit diffusion. These results suggest different antifouling additives are needed in different trays and perhaps at different times. Perturbations applied to the dissolved oxygen concentration in the feedstock demonstrated that even at parts-per-million (ppm) levels, dissolved oxygen had a substantial accelerat-

ing effect on film growth. These findings highlight the importance of considering oxygen chemistry in the modeling of polymer fouling within distillation columns. The developed fouling model provides insights into the role of oxygen in the fouling process and its impact on film growth, contributing to a better understanding of fouling phenomena in industrial distillation operations.

## Acknowledgement

This work at MIT is sponsored by Dow Inc. H. P. is funded by the Think Global Trust Scholarship. The authors acknowledge the MIT SuperCloud and Lincoln Laboratory Supercomputing Center[38] for providing computing resources that have contributed to the research results reported within this paper.

## Supporting Information Available

Supplementary Information related to this article can be found at [TBD]. The supplementary information includes quantum chemical calculation schemes and transition state geometries, fouling model construction and simulation details, and additional model analyses. All the automated scripts used for model generation, simulation, and analyses can be found in the GitHub repository: `https://github.com/hwpang/PolymerFoulingModeling`, including the mechanism files in CHEMKIN format and .rms format. The Aspen model, all the quantum chemical calculation output files, and all the model simulation and rate of production output results can be found at `https://zenodo.org/doi/10.5281/zenodo.8349778`.

## References

(1) Coletti, F.; Crittenden, B. D.; Macchietto, S. *Crude Oil Fouling*; Elsevier, 2015; pp 23–50.

(2) Busch, M. Modeling Kinetics and Structural Properties in High-Pressure Fluid-Phase Polymerization. *Macromolecular Theory and Simulations* **2001**, *10*, 408–429.

(3) Yang, J.; Serratos, M. G. J.; Fari-Arole, D. S.; Müller, E. A.; Matar, O. K. Crude oil fouling: Fluid dynamics, reactions and phase change. *Procedia IUTAM* **2015**, *15*, 186–193.

(4) Fries, S.; Castañeda-Zúñiga, D. M.; Duchateau, J.; Neuteboom, P.; Porras, C. T.; Busch, M. Fouling in the High Pressure LDPE Process: Experimental and Computational Investigation Approach. Macromolecular Symposia. 2016; pp 78–86.

(5) Yang, J. Computational fluid dynamics studies on the induction period of crude oil fouling in a heat exchanger tube. *International Journal of Heat and Mass Transfer* **2020**, *159*, 120129.

(6) Pang, H.-W.; Forsuelo, M.; Dong, X.; Hawtof, R. E.; Ranasinghe, D. S.; Green, W. H. Detailed Multiphase Chemical Kinetic Model for Polymer Fouling in a Distillation Column. *Industrial & Engineering Chemistry Research* **2023**, *62*, 14266–14285.

(7) Welch, L.; Swaney, M.; Gleason, A.; Beckwith, R.; Howe, R. Initiation and growth of butadiene resinous polymers. *Industrial & Engineering Chemistry* **1947**, *39*, 826–829.

(8) Watkinson, A. P. Chemical reaction fouling of organic fluids. *Chemical Engineering & Technology: Industrial Chemistry-Plant Equipment-Process Engineering-Biotechnology* **1992**, *15*, 82–90.

(9) Wilson, D. I.; Watkinson, A. P. A study of autoxidation reaction fouling in heat exchangers. *The Canadian Journal of Chemical Engineering* **1996**, *74*, 236–246.

(10) Watkinson, A.; Wilson, D. Chemical reaction fouling: A review. *Experimental Thermal and Fluid Science* **1997**, *14*, 361–374.

(11) Sundaram, B. N. The effects of oxygen on synthetic crude oil fouling. Ph.D. thesis, University of British Columbia, 1998.

(12) Watkinson, A. P.; Navaneetha-Sundaram, B.; Posarac, D. Fouling of a sweet crude oil under inert and oxygenated conditions. *Energy & Fuels* **2000**, *14*, 64–69.

(13) Wilson, D. I. Model experiments of autoxidation reaction fouling. Ph.D. thesis, University of British Columbia, 1994.

(14) Aspen Plus. `https://www.aspentech.com/en/products/engineering/aspen-plus`, Accessed 2023-11-29.

(15) Gao, C. W.; Allen, J. W.; Green, W. H.; West, R. H. Reaction Mechanism Generator: Automatic construction of chemical kinetic mechanisms. *Computer Physics Communications* **2016**, *203*, 212–225.

(16) Liu, M.; Grinberg Dana, A.; Johnson, M. S.; Goldman, M. J.; Jocher, A.; Payne, A. M.; Grambow, C. A.; Han, K.; Yee, N. W.; Mazeau, E. J., et al. Reaction Mechanism Generator v3. 0: Advances in Automatic Mechanism Generation. *Journal of Chemical Information and Modeling* **2021**, *61*, 2686–2696.

(17) Johnson, M. S.; Dong, X.; Grinberg Dana, A.; Chung, Y.; Farina Jr, D.; Gillis, R. J.; Liu, M.; Yee, N. W.; Blondal, K.; Mazeau, E., et al. RMG Database for Chemical Property Prediction. *Journal of Chemical Information and Modeling* **2022**, *62*, 4906–4915.

(18) Reaction Mechanism Generator (RMG). `https://github.com/ReactionMechanismGenerator/RMG-Py`, Accessed 2023-11-29.

(19) Anderson, R.; Friedel, R.; Storch, H. Fischer-Tropsch reaction mechanism involving stepwise growth of carbon chain. *The Journal of Chemical Physics* **1951**, *19*, 313–319.

(20) Han, K.; Green, W. H. A fragment-based mechanistic kinetic modeling framework for complex systems. *Industrial & Engineering Chemistry Research* **2018**, *57*, 14022–14030.

(21) Johnson, M. S.; Pang, H.-W.; Payne, A. M.; Green, W. H. ReactionMechanismSimulator.jl: A Modern Approach to Chemical Kinetic Mechanism Simulation and Analysis. *ChemRxiv* **2023**, Submission 2023-04-18. Accessed 2023-11-29.

(22) Reaction Mechanism Simulator (RMS). `https://github.com/ReactionMechanismGenerator/ReactionMechanismSimulator.jl`, Accessed 2023-11-29.

(23) Battino, R.; Rettich, T. R.; Tominaga, T. The solubility of oxygen and ozone in liquids. *Journal of Physical and Chemical Reference Data* **1983**, *12*, 163–178.

(24) Billet, R.; Schultes, M. Prediction of mass transfer columns with dumped and arranged packings: updated summary of the calculation method of Billet and Schultes. *Chemical Engineering Research and Design* **1999**, *77*, 498–504.

(25) Bell, I. H.; Wronski, J.; Quoilin, S.; Lemort, V. Pure and Pseudo-pure Fluid Thermophysical Property Evaluation and the Open-Source Thermophysical Property Library CoolProp. *Industrial & Engineering Chemistry Research* **2014**, *53*, 2498–2508.

(26) Chung, Y.; Gillis, R. J.; Green, W. H. Temperature-dependent vapor–liquid equilibria and solvation free energy estimation from minimal data. *AIChE Journal* **2020**, *66*, e16976.

(27) Chung, Y.; Vermeire, F. H.; Wu, H.; Walker, P. J.; Abraham, M. H.; Green, W. H. Group contribution and machine learning approaches to predict Abraham solute parameters, solvation free energy, and solvation enthalpy. *Journal of Chemical Information and Modeling* **2022**, *62*, 433–446.

(28) Rice, S. A. *Diffusion-limited reactions*; Elsevier, 1985.

(29) Flegg, M. B. Smoluchowski reaction kinetics for reactions of any order. *SIAM Journal on Applied Mathematics* **2016**, *76*, 1403–1432.

(30) Speth, R. L.; Green, W. H.; MacNamara, S.; Strang, G. Balanced splitting and rebalanced splitting. *SIAM Journal on Numerical Analysis* **2013**, *51*, 3084–3105.

(31) Deen, W. M. *Analysis of transport phenomena*; Oxford University Press, 2011.

(32) Automated Rate Calculator (ARC). `https://github.com/ReactionMechanismGenerator/ARC`, Accessed 2023-11-29.

(33) RDKit: Open-source cheminformatics. `https://www.rdkit.org`, Accessed 2023-11-29.

(34) Frisch, M. J. et al. Gaussian 09 Revision E.01. Gaussian Inc. Wallingford CT 2009.

(35) Frisch, M. J. et al. Gaussian 16 Revision C.01. 2016; Gaussian Inc. Wallingford CT.

(36) Montgomery Jr, J. A.; Frisch, M. J.; Ochterski, J. W.; Petersson, G. A. A complete basis set model chemistry. VI. Use of density functional geometries and frequencies. *The Journal of Chemical Physics* **1999**, *110*, 2822–2827.

(37) Merchant, S. S.; Zanoelo, E. F.; Speth, R. L.; Harper, M. R.; Van Geem, K. M.; Green, W. H. Combustion and pyrolysis of iso-butanol: Experimental and chemical kinetic modeling study. *Combustion and Flame* **2013**, *160*, 1907–1929.

(38) Reuther, A. et al. Interactive supercomputing on 40,000 cores for machine learning and data analysis. 2018 IEEE High Performance Extreme Computing Conference (HPEC). 2018; pp 1–6.

# TOC Graphic